Top Catal (2017) 60:110–122
DOI 10.1007/s11244-016-0723-7

ORIGINAL PAPER

# CO and VOCs Catalytic Oxidation Over Alumina Supported Cu–Mn Catalysts: Effect of Au or Ag Deposition

**T. Tabakova[1] · E. Kolentsova[2] · D. Dimitrov[2] · K. Ivanov[2] · M. Manzoli[3] · A. M. Venezia[4] · Y. Karakirova[1] · P. Petrova[1] · D. Nihtianova[5] · G. Avdeev[6]**

Published online: 29 September 2016


**Abstract** Alumina supported Cu–Mn mixed oxide with Cu/Mn molar ratio 2:1 was used as a support of gold and silver catalysts for oxidation of CO, methanol and dimethylether. Different techniques (XRD, HRTEM, XPS, FTIR, EPR, and TPR) were used to investigate structure–reactivity relationship. A strong effect of the nature of the promoters on the catalytic behaviour was observed. Superior catalytic activity in oxidation of CO was measured after addition of Au, while modification by Ag affected very slightly the CO oxidation activity of Cu/Mn 2:1 sample. Both Au and Ag have beneficial effect on $CH_3OH$ oxidation activity of Cu–Mn mixed oxides. The combination of the good redox properties of Cu–Mn mixed oxides and gold nanoparticles has proved to be an advantageous approach for developing new catalytic formulations with high effectiveness to eliminate different type pollutants in waste gases from formaldehyde production. The use of high surface area support is beneficial for the stabilization of gold particles in a highly dispersed state and contributes for economic viability in case of practical applications, because of the composition of this catalytic system, that is mostly alumina (80 %).

**Keywords** Gold catalysts · CO oxidation · VOCs abatement · Mixed Cu–Mn oxides

## 1 Introduction

Increasing concerns about the growing emissions of carbon monoxide and volatile organic compounds (VOCs) in the atmosphere stimulate great research efforts for development of highly efficient materials for catalytic oxidation of these air pollutants [1, 2]. Supported noble metals or transition metal oxides are mainly used as catalysts for total VOC oxidation. Noble metals are expensive, but they demonstrate high specific activity, stability and could be regenerated [3, 4]. Currently, it is well known that gold in highly dispersed state exhibits very high activity in numerous environmental catalytic processes [5, 6]. The activity of gold-based catalysts is dependent not only on the size of the supported gold particles, but also on their interaction with the support.

Transition metal oxide catalysts are less active than noble metals at low temperatures, however, due to their lower price, they are intensively studied as a suitable alternative for replacing noble metal catalysts [7]. Mixed

**Electronic supplementary material** The online version of this article (doi:10.1007/s11244-016-0723-7) contains supplementary material, which is available to authorized users.

✉ T. Tabakova
tabakova@ic.bas.bg

[1] Institute of Catalysis, Bulgarian Academy of Sciences, Acad. G. Bonchev St., Block 11, 1113 Sofia, Bulgaria

[2] Department of Chemistry, Agricultural University, 4000 Plovdiv, Bulgaria

[3] Department of Chemistry and NIS Interdepartmental Centre, University of Turin, 10125 Turin, Italy

[4] Institute for Nanostructured Materials (ISMN)-CNR, 90146 Palermo, Italy

[5] Institute of Mineralogy and Crystallography, Bulgarian Academy of Sciences, 1113 Sofia, Bulgaria

[6] Institute of Physical Chemistry, Bulgarian Academy of Sciences, 1113 Sofia, Bulgaria

metal oxides have shown a very good performance in VOCs oxidation [8–11]. Among transition metal oxides, Cu–Mn mixed oxides are one of the most widely used catalysts for oxidation of CO [12–16], as well as of different VOCs [17–21].

Considering the high CO oxidation activity at low temperature of both nanosized gold-based catalysts and Cu–Mn mixed oxides, Solsona et al. prepared Au-containing Hopcalite catalysts by a co-precipitation method [22]. The $CuMnO_x$ sample with 3 wt% Au demonstrated significant increase of CO oxidation rate and improved resistance to deactivation. Cole et al. used deposition–precipitation procedure for modifying Cu–Mn oxide catalysts with Au [23]. The composition with 1 wt% Au was the most favorable to improve the CO oxidation activity and caused the greatest effect on reducibility. The addition of Au to co-precipitated Hopcalite also influenced the performance for total propane oxidation, in terms of both activity and stability [24]. Lamb et al. included silver in the original formulations of Hopcalite, to enhance the oxidation of CO [25].

Recently, some of us investigated the relationship between Cu/Mn molar ratio, thermal treatment of the precursor and amount of active component of alumina supported Cu–Mn catalysts and the activity for oxidation of some air pollutants from formaldehyde production [26]. The catalytic oxidation of $CH_3OH$ to formaldehyde is an important industrial process in which the waste gases contain small amounts of $CH_3OH$, $(CH_3)_2O$ and CO. It was shown that the impregnation of $\gamma$-$Al_2O_3$ with 20 wt% Cu–Mn mixed oxide is an appropriate method for the preparation of active and cost-effective catalysts for combustion of waste gases from formaldehyde production. High-surface area $\gamma$-$Al_2O_3$ is a widely used support for noble metals Pt, Pd and Rh for production of highly efficient catalysts in VOC abatement. In contrast, Au supported on alumina demonstrated a low catalytic activity in the combustion of VOCs [27]. Ivanova et al. tested $Au/Al_2O_3$ in the total oxidation of a mixture of light hydrocarbons and CO in order to study the applicability of this catalyst in the reduction of cold start emissions [28]. The authors found that alumina alone is not a suitable support and the presence of another reducible oxide is needed to facilitate oxygen spillover over the catalyst surface.

The aim of this work is to combine the favorable features of transition metal oxides and noble metals (NMs) in order to develop new catalytic formulations of improved efficiency and economic viability. In this connection, the role of Au and Ag on the structural, electronic, reductive and catalytic properties of $Cu–Mn/Al_2O_3$ catalysts for simultaneous oxidation of CO, methanol and dimethylether (DME) has been deeply investigated.

## 2 Experimental

### 2.1 Catalyst Preparation

The mixed oxide with Cu/Mn molar ratio 2:1 was prepared by wet impregnation of $\gamma$-alumina (0.6–1.0 mm grain size). The selection of such ratio is based on our recent findings about successful oxidation of CO and $CH_3OH$ over alumina supported Cu/Mn with molar ratio 2:1 [26]. The total amount of transition metal oxides phase was 20 wt%. The alumina support was calcined at 500 °C for 2 h before impregnation. An aqueous solution of copper and manganese nitrates with desired ratio was added to a defined amount of $\gamma$-alumina at room temperature (RT). The support remained immersed in this solution at 80 °C for 12 h. The impregnated sample was then dried and calcined according to the following sequence: drying at RT for 12 h, heating at 120 °C for 10 h, calcining at 450 °C for 4 h after increasing the temperature from 120 °C by 10 °C/min.

The Au- and Ag-containing catalysts were synthesized by deposition–precipitation of 2 wt% metal on $Cu–Mn/Al_2O_3$. The support was suspended in water and the deposition was carried out by simultaneous addition of an aqueous solution of $HAuCl_4$ or $AgNO_3$, and $Na_2CO_3$ at 60 °C and pH 7.0 (for Au) or 9.0 (for Ag). After aging at 60 °C for 1 h, the materials were filtered and carefully washed until removal of $Cl^-$or $NO_3^-$ ions. The thermal treatment included drying under vacuum at 80 °C and calcination in air at 400 °C for 2 h.

### 2.2 Catalytic Activity Measurements

The catalytic measurements related to the single compound oxidation were carried out on continuous flow equipment with a four-channel isothermal stainless steel reactor, containing 1.0 ml catalyst at atmospheric pressure and space velocity (GHSV) of 10,000 $h^{-1}$, allowing simultaneous examination of four catalysts under the same conditions. The flow of ambient air (40–50 % humidity) and CO (final concentration 1.5 %) were fed using mass flow controllers (GFC Mass Controller AABORG, Germany). Liquid methanol was dosed by Ismatec micro-dosage pump and additional air was added before reaching the preheater to final concentration of methanol 1.5 %. DME (final concentration 0.8–1.0 %) was obtained by dehydration of methanol on $\gamma$-$Al_2O_3$ in tubular isothermal reactor.

A two stage equipment for the simultaneous oxidation of all compounds (CO, $CH_3OH$ and DME) under conditions as close as possible to the industrial set-up was used: (1) flow-line equipment with stainless steel pseudo-isothermal reactor for methanol selective oxidation [30] and (2) flow-line equipment with a four-channel isothermal stainless

steel reactor, described above, for the oxidation of by-products (CO 1.2–1.3 %, methanol 0.2–0.3 %, DME 0.5–0.6 % and water 3.0–3.2 %). Detailed description is reported elsewhere [30]. Gas mixtures at both input and output of the reactor were analyzed with a gas chromatograph HP 5890 Series II, equipped with FID and TCD detectors, column Porapak Q (for methanol, $CO_2$ and DME) and column MS-5A (for CO, oxygen and nitrogen). The degree of conversion of all compounds was used for evaluation of catalysts' activity, in percentages.

### 2.3 Catalyst Characterization

Nitrogen adsorption–desorption isotherms were measured at −196 °C with a Quantachrome Instruments NOVA 1200e (USA) apparatus. Pore diameter and total pore volume were determined in accordance with the Gurvich rule at a relative pressure close to 0.99, while the specific surface areas ($S_{BET}$) were estimated through the Brunauer, Emmett and Teller (BET) method in a standard pressure range $p/p_0 = 0.10–0.30$.

The phase composition was characterized by X-ray powder diffraction (XRD) using a PANalytical Empyrean equipped with a multichannel detector (Pixel 3D) using (Cu Kα 45 kV–40 mA) radiation in the 20°–115° 2$\theta$ range, with a scan step of 0.01° for 20 s.

Transmission electron microscopy (TEM) and high resolution TEM (HRTEM) were performed by a JEOL 2100 instrument at accelerating voltage 200 kV, equipped with a XEDS spectrometer (Oxford instruments, X-max$^N$ 80T) and STEM module. Selected Area Electron Diffraction (SAED) was also employed to have information on the nature of the crystalline phases. The samples were prepared by grinding and dispersing the powders in ethanol by ultrasonic treatment for 6 min. The suspensions were dripped on standard holey carbon/Ni grids.

X-ray photoelectron spectroscopy (XPS) analyses were performed with a VG Microtech ESCA 3000 Multilab, equipped with a dual Mg/Al anode. The spectra were excited by the unmonochromatized Al Kα source (1486.6 eV) run at 14 kV and 15 mA. The constant charging of the samples was corrected by referencing all the energies to the C 1 s peak energy set at 285.1 eV, arising from adventitious carbon. A detailed description of experimental conditions and analyses of the peaks conditions is already reported in Ref. [29].

Fourier transformed infrared (FTIR) spectra were recorded in transmission mode at a resolution of 2.0 cm$^{-1}$ and by acquiring 60 scans on a Perkin–Elmer 2000 spectrometer (equipped with a MCT detector). The samples in self-supporting pellets were introduced in a cell allowing thermal treatments in controlled atmosphere and spectrum scanning at controlled temperature (from −196 °C up to RT). An oxidative treatment was performed before CO adsorption, as follows: heating from RT up to 200 °C under outgassing; inlet of 20 mbar of $O_2$ and heating up to 400 °C; at 400 °C the oxygen was changed three times (20 mbar for 10 min each run), cooling down to RT in $O_2$ and finally outgassing. The reductive treatment was carried out after the oxidation by heating from RT to 250 °C in 20 mbar of $H_2$ and the hydrogen (10 mbar) was changed three times during a 10 min total time. Then the sample was cooled to RT under outgassing. The spectrum of the sample before the inlet of CO was used as background for each spectrum. All reported spectra were background subtracted and normalized to the weight of the pellets.

Electron paramagnetic resonance (EPR) spectra were recorded at JEOL JES-FA 100 EPR spectrometer operating in X-band with standard TE011 cylindrical resonator under the following conditions: modulation frequency 100 kHz, microwave power 1 mW, modulation amplitude 0.2 mT, sweep 500 mT, time constant 0.3 s and sweeping time 4 min. The samples were placed in quartz cuvettes and were fixed in the cavity center.

Temperature programmed reduction (TPR) measurements were carried out in a flow system using hydrogen-argon mixture (10 % $H_2$) with flow rate 24 mL min$^{-1}$. The amount of the sample was 0.05 g. The temperature was linearly increased at a rate of 15 °C min$^{-1}$. A cooling trap (−40 °C) for removing water formed during reduction was mounted in the gas line prior to the thermal conductivity detector.

## 3 Results and Discussion

### 3.1 Catalytic Activity Measurements

The temperature dependence of the catalytic activity in terms of CO, $CH_3OH$ and DME conversion is compared in Fig. 1 for the studied samples. Bare Cu–Mn/$Al_2O_3$ was also examined for comparison. A strong effect of the nature of promoters on the catalytic behaviour was observed. In particular, a superior catalytic activity in CO oxidation was measured after addition of Au, indeed the complete CO conversion was achieved at 40 °C (Fig. 1a). In contrast, Ag/Cu–Mn and alumina supported Cu–Mn samples demonstrated low ability to oxidize CO at RT. These samples reached maximum CO conversion at about 180 °C. The modification by Ag affected very slightly CO oxidation activity of Cu/Mn 2:1 sample. On the contrary, both Au and Ag have beneficial effect on $CH_3OH$ oxidation activity of Cu–Mn mixed oxides; however the role of Au was much more favorable (Fig. 1b). The light-off curves of CO and methanol oxidation over Au/Cu–Mn catalyst were shifted to lower temperature with respect to that of the

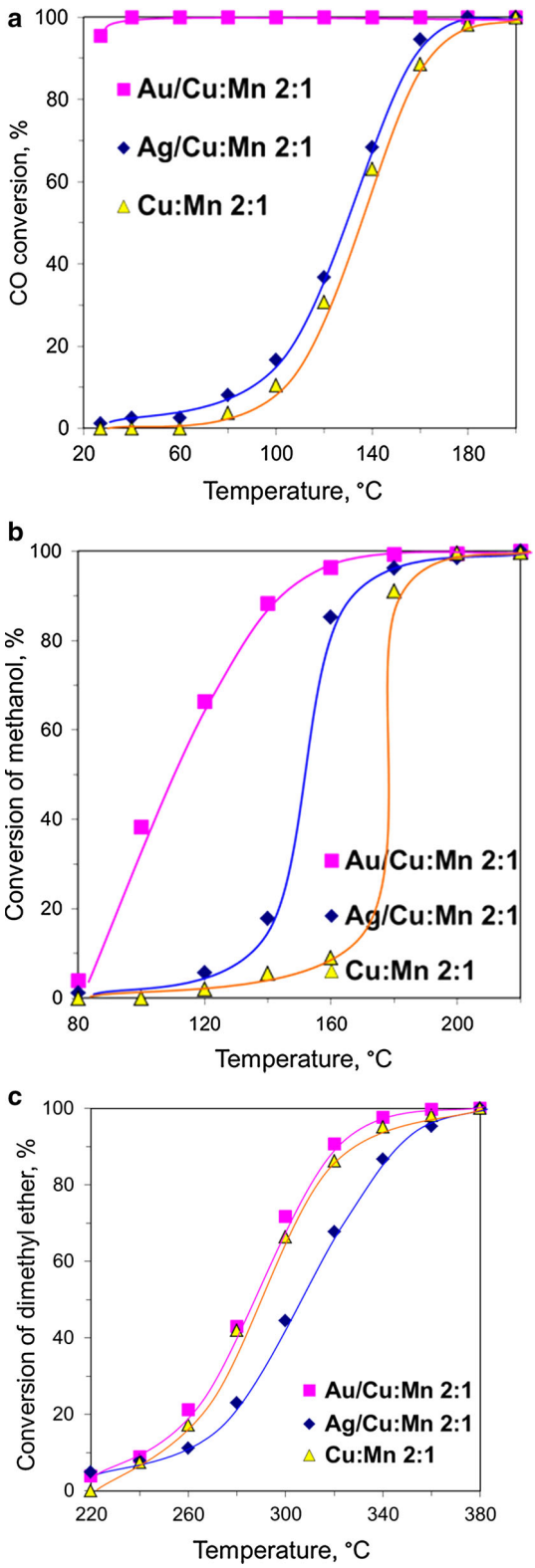


**Fig. 1** Temperature dependence of oxidation of CO (section **a**), $CH_3OH$ (section **b**) and DME (section **c**) over the studied samples

other two samples. This behavior is better pointed out by comparison of the $T_{50}$ conversion values of $CH_3OH$ (i.e. the temperature at which 50 % conversion was reached): 110 °C over Au/Cu–Mn, 145 °C over Ag/Cu–Mn and 178 °C over Cu–Mn. The doping with Au had insignificant impact on the DME oxidation, while addition of Ag caused decreased activity (Fig. 1c).

The results for the simultaneous oxidation of a CO, $CH_3OH$ and DME mixture over the alumina supported Cu–Mn 2:1 sample and over the Au-promoted sample are compared in Fig. 2, sections a and b, respectively. It was chosen to carry out the experiments only over the gold-containing sample because of its promising catalytic

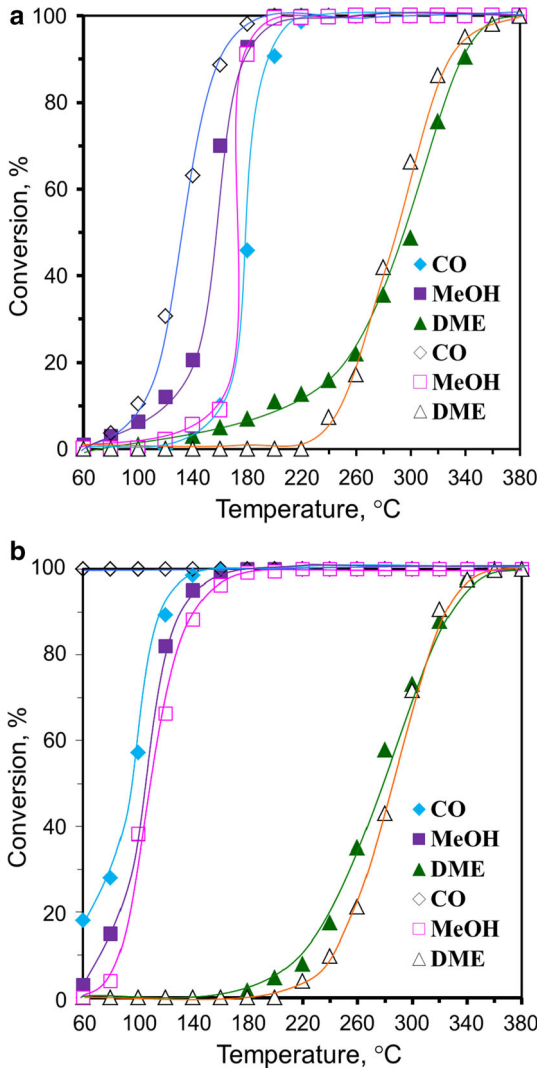


**Fig. 2** Temperature dependence of oxidation of CO, $CH_3OH$ and DME alone (*empty symbols*) or in mixture (*full symbols*) over Cu–Mn 2:1 (section **a**) and Au/Cu–Mn 2:1 (section **b**)

behavior for CO and VOCs abatement. The oxidation of CO at low temperature was significantly affected by the presence of $CH_3OH$ and DME, and this effect was much stronger over the Au-doped catalyst. The data could be interpreted in terms of inhibited CO oxidation in the presence of organic molecules. In contrast, the presence of CO has no impact on the methanol and DME oxidation. The total CO and $CH_3OH$ conversion over gold-containing sample was reached almost at the same temperature (about 160 °C) with slight preference for CO oxidation. It could be hypothesized that the oxidation of these two molecules occurred on the same active sites. However, the oxidation of methanol over Cu–Mn 2:1 was shifted to lower temperature in comparison with CO oxidation. In this case, it could be assumed that CO and $CH_3OH$ were adsorbed competitively: indeed the adsorption of methanol hindered CO adsorption. The degree of methanol conversion at 180 °C was 92 %, while that of CO was below 50 %. The complete CO oxidation was achieved after total methanol oxidation. All these findings revealed a beneficial promotion by gold that is related to the strong ability of gold nanoparticles to adsorb and activate CO molecules. As it was already noted, the oxidation of methanol over Au/Cu–Mn catalyst is not influenced by the presence of CO and the total conversion of both gases was downshifted of about 50° if compared to the non-promoted sample.

Moreover, the comparison of the activity for the simultaneous oxidation of a CO, $CH_3OH$ and DME mixture of Au-promoted sample with the one of a commercial Pt/$Al_2O_3$ catalyst (Fig. S1) points out the promising application of Au/Cu–Mn/alumina materials in elimination of different type pollutants in waste gases.

### 3.2 Catalyst Characterization: Structure–Reactivity Relationship

Some textural properties of the samples are listed in Table 1. The impregnation of γ-alumina with mixed Cu–Mn solution led to the expected decrease of the surface area. Additionally, the deposition of Au and Ag caused the same effect. The analysis of the adsorption–desorption isotherm and of the corresponding pore size distribution, both related to the alumina supported Cu/Mn 2:1 sample, indicated the presence of very well defined mesopores with narrow pore size distribution. These textural properties remained almost the same after doping with Au and Ag.

**Table 1** Texture characteristics of the samples

| Sample | S, $m^2/g$ | $V_{total}$, $cm^3/g$ | $D_{av.}$, nm |
|---|---|---|---|
| $Al_2O_3$ | 219 | 0.40 | 7.4 |
| Cu–Mn 2:1 | 177 | 0.31 | 7.1 |
| Au/Cu–Mn 2:1 | 143 | 0.28 | 7.7 |
| Ag/Cu–Mn 2:1 | 164 | 0.31 | 7.6 |

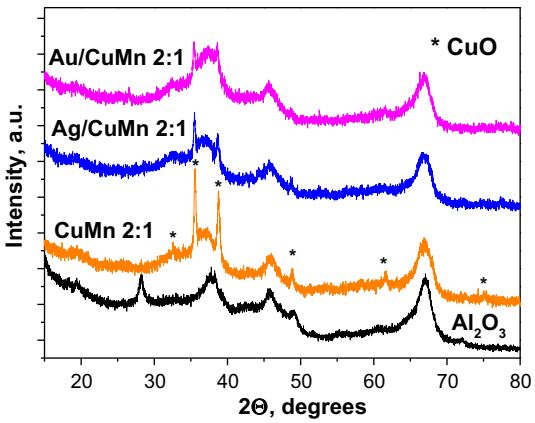


**Fig. 3** Powder XRD patterns of the examined samples

The X-ray powder diffraction patterns of the samples are shown in Fig. 3. The diffraction peaks due to bare γ-alumina support were detected in the XRD patterns of all materials. Sharp reflections at $2\theta = 35.6°$, 38.8°, 48.6° and 61.8° assigned to the CuO phase (marked with *, JCPDS 02-1040) were clearly identified in the diffractogram related to the Cu–Mn sample with ratio 2:1. The shape of the peaks indicated high degree of crystallinity of the CuO particles. The average crystallite size, calculated from the X-ray line broadening of the peaks at $2\theta = 35.6$ and 38.8°, was about 30 nm. However, basing on TG/DTA measurements performed recently on this sample [31], the presence of a Cu–Mn spinel phase was suggested. The analysis of the DTG and DTA curves allowed concluding that the last weight loss at 303 °C was associated to the formation of a highly dispersed mixture of CuO and Cu–Mn spinel. No reflections due to such phase were observed in the XRD patterns, probably due to the relatively small crystallite size and/or its high dispersion. Clarke et al. attributed the increase of the relative weight loss observed for a mixture of CuO and $MnCO_3$ calcined at 415 °C to the $Cu^{2+}$ incorporation and to the formation of a nanocrystalline $CuMn_2O_4$ material [16]. Additionally, the existence of a Cu–Mn spinel phase is in agreement with the Cu–Mn–O phase diagram published recently [32]. The intensity of CuO reflections significantly decreased after modification with Au and Ag. However, diffraction peaks assignable to the presence of crystalline Au or Ag were not discernible. The most intense peaks of Au and Ag, associated with the (1 1 1) lattice plane, are known to be located at $2\theta = 38.2°$. In this case, the strong CuO (1 1 1) reflection lying at the same angle would preclude their exact identification even if they existed. However, the lack of diffraction peaks at $2\theta = 44.4°$ and 62.6° allows one to assume a high dispersion of the metallic particles. Well defined crystalline

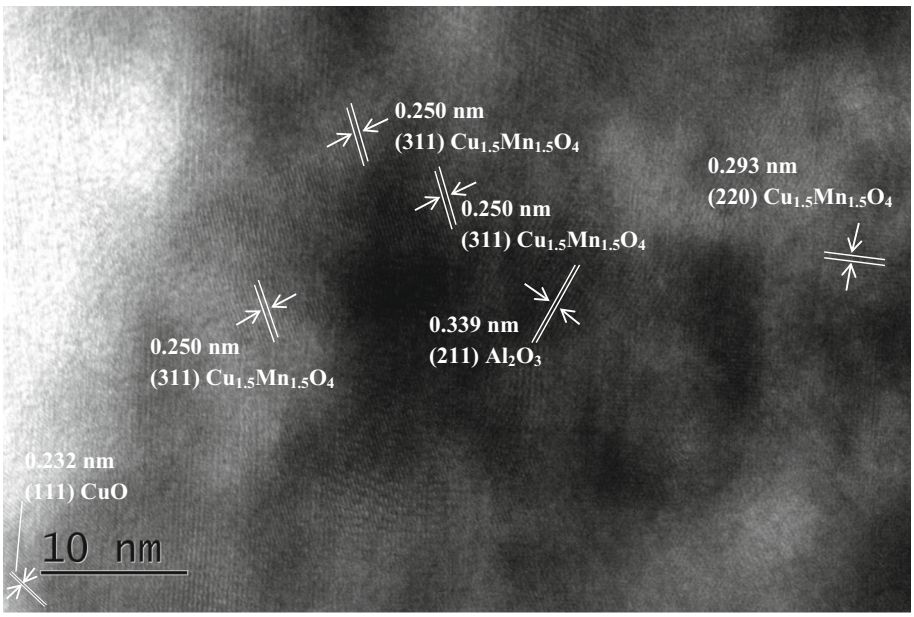


**Fig. 4** HRTEM image in bright field mode of the Cu/Mn 2:1 sample. Instrumental magnification: 400,000X

lattice fringes were observed by HRTEM in the bright field image of bare Cu–Mn with ratio 2:1 supported on alumina (Fig. 4). The distances among the fringes were measured and the spacing of these fringes (0.240 nm) closely corresponds to the (2 2 2) lattice plane of $Cu_{1.5}Mn_{1.5}O_4$. Moreover, other lattice interplanar distances (0.140 and 0.293 nm, respectively) related to the (5 3 1) and (2 2 0) planes of $Cu_{1.5}Mn_{1.5}O_4$ were determined, thus confirming the formation of spinel phase. Kondrat et al. have correlated the CO oxidation activity with the presence of the Cu–Mn spinel and have found that the higher is the content, the higher is the activity [33].

Further, the analysis was focused on the most active gold-based catalyst and the SAED pattern, where the coexistence of Au, CuO and $Cu_{1.5}Mn_{1.5}O_4$ nanocrystalline phases is demonstrated in Fig. 5. In addition, the elemental mapping analysis clearly revealed that all elements investigated (Cu, Mn, Al, O and Au) are homogeneously distributed on the support (Fig. 6). The presence of finely dispersed gold particles with size of about 1–2 nm was suggested.

The oxidation state of the surface species of Cu–Mn 2:1 sample in their as prepared form before and after Au deposition was studied by XPS. The main results from the

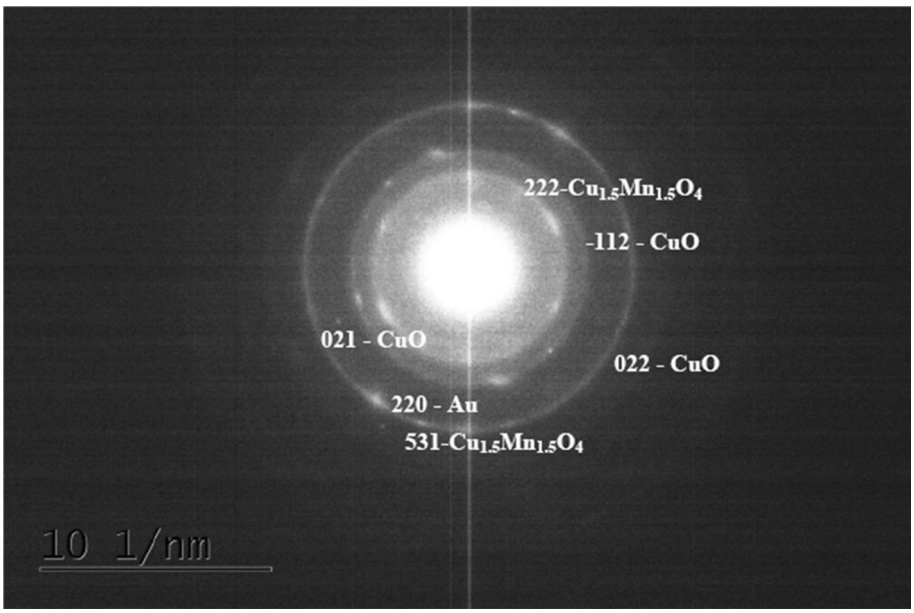


**Fig. 5** SAED pattern of the Au/Cu–Mn 2:1 sample

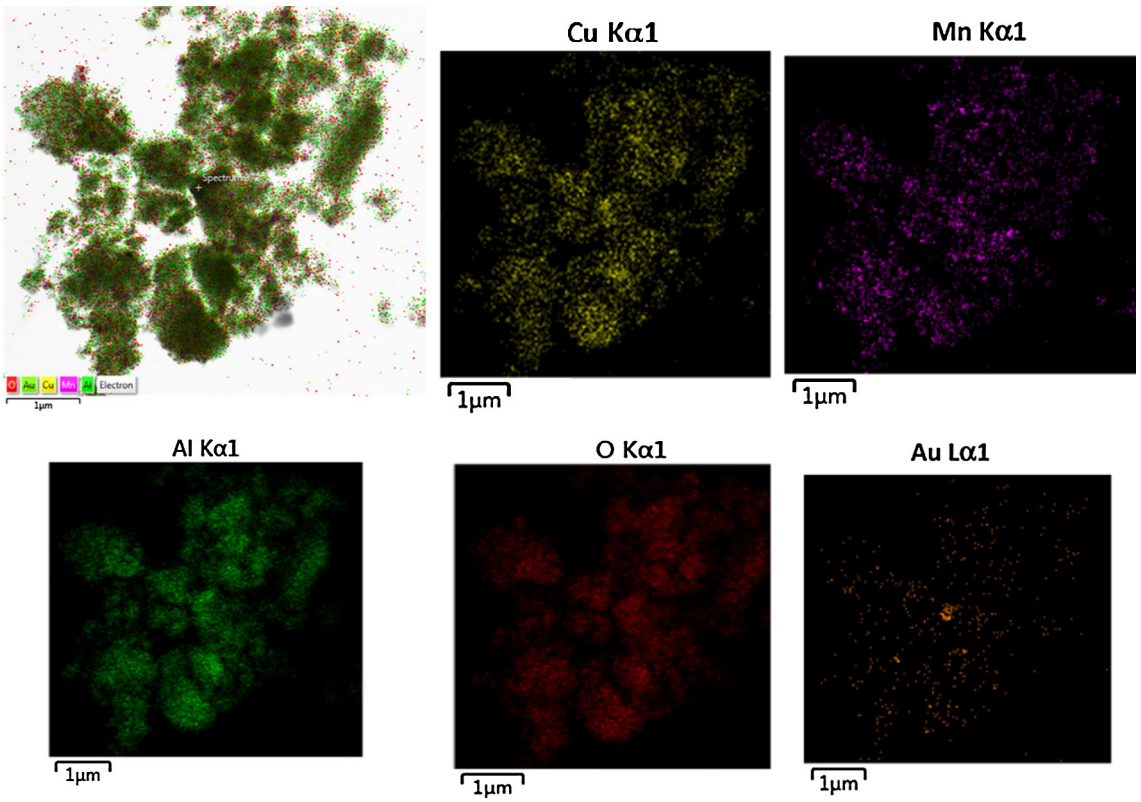


**Fig. 6** Representative STEM image of the Au/Cu–Mn 2:1 catalyst and relative XEDS mapping showing copper (*yellow*), manganese (*violet*), oxygen (*red*), aluminum (*green*) and gold (*orange*) distribution

**Table 2** XPS data of the samples

| Sample | BE (eV) Cu $2p_{3/2}$ | BE (eV) Mn $2p_{3/2}$ | BE (eV) Al 2p | BE (eV) Au $4f_{7/2}$ | Cu/Mn | Cu/Al | Au/Cu | Au/(Cu + Mn) |
|---|---|---|---|---|---|---|---|---|
| Cu/Mn 2:1 | 933.0 | 642.6 | 74.7 | – | 2.9 | 0.06 | – | – |
| Au/Cu–Mn 2:1 | 933.2 | 642.5 | 74.8 | 84.8 | 2.5 | 0.04 | 0.06 | 0.04 |

XP analysis are summarized in Table 2. As concerns the state of copper and manganese, the curve fitting analysis indicated that Cu(I), Cu(II), Mn(III) and Mn(IV) species were simultaneously present in both samples. These results are in good agreement with HRTEM evidences, confirming the formation of a spinel phase. The Cu $2p_{3/2}$ spectra of

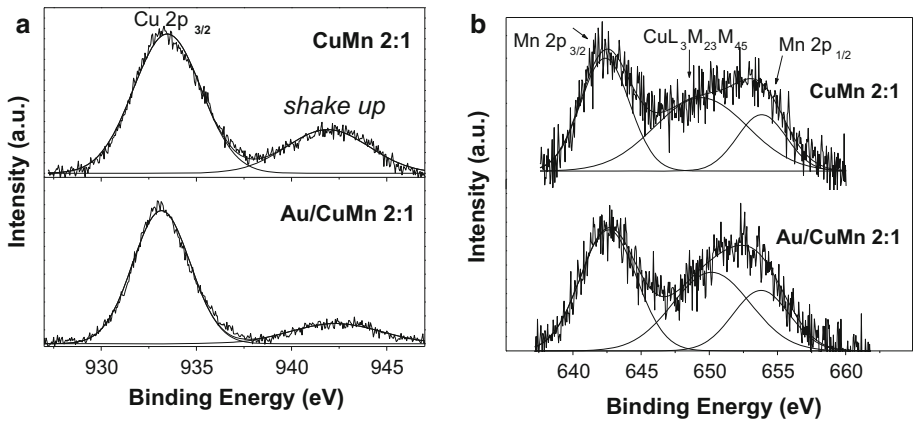


**Fig. 7** XPS spectra of Cu 2p (**a**) and Mn 2p (**b**) of Cu–Mn 2:1 and Au/Cu–Mn 2:1 samples

alumina supported Cu–Mn phase and gold-containing samples are shown in Fig. 7a. According to the Cu $2p_{3/2}$ binding energy value of 933.2–933.4 eV and to the occurrence of shake up peaks typical of Cu(II), copper is mainly present as CuO [34]. However, the intensity ratio of the shake up feature with respect to the main Cu $2p_{3/2}$, being smaller than what expected for a pure Cu(II) species, suggested a coexisting Cu(I) oxide. A further decrease of such relative intensity ratio was in agreement with an increase of the low valence copper component in the gold loaded sample. The interpretation of XP spectra of $MnO_x$ in terms of the actual Mn oxidation state is rather complicated because of the variety of possible oxidation states, some of them characterized by multiplet splitting [35]. The obtained Mn $2p_{3/2}$ binding energy of 642.5 ± 0.1 eV is typical of Mn(IV) [35, 36]. However, the rather broad linewidth of the peak (4.4 eV) suggested a contribution from Mn(III). Additionally, it should be mentioned that the Mn 2p peak overlaps with the Auger component $CuL_3$-$M_{23}M_{45}$ (Fig. 7b). By using appropriate fitting, restraining the distance between the two spin orbit components and fixing equal linewidths for each spin orbit component it was possible to evaluate atomic ratios between Cu and Mn. The Cu/Al ratios were also calculated (see Table 2). The decrease of the Cu/Mn ratio upon Au deposition can be seen directly from the Mn 2p spectrum where the Cu Auger component, relatively to the Mn 2p peaks is smaller in the gold-containing sample.

The position of Au $4f_{7/2}$ peak at 84.8 eV indicated the presence of positively charged gold species. According to HRTEM observations, this result is consistent with high dispersion of gold after deposition on alumina supported Cu–Mn mixed oxides, because the presence of structural defects may facilitate nucleation of gold clusters [37]. The role of cationic gold for increased activity in CO and VOCs oxidation was discussed by many authors [6, 38, 39]. Higher activity for methanol, ethanol and 2-propanol conversion was ascribed to the presence of $Au^{\delta+}$ species, rather than $Au^0$ species, by Minicò et al. [40]. Very recently, Nikolaev et al. studied bimetallic Au–Cu/$Al_2O_3$ catalysts and observed that the formation of $Au^{\delta+}$ was accompanied by reduction of CuO, as evidenced by a decrease in the relative area of the XP peak of $Cu^{2+}$ [41]. Similar finding were reported by Duh et al. that found CuO conversion to $Cu_2O$ after deposition of Au on a CuO/$TiO_2$ catalyst, as well as a positive shift of Au 4f peaks [42]. Analyzing the calculated atomic ratios between Cu and Mn for both Cu–Mn 2:1 and Au-containing samples, it was obvious the decreased values for Cu/Mn and Cu/Al ratios after modification with Au, while the atomic ratio Mn/Al was nearly the same. This observation is consistent with the findings of Cole et al. about the appearance of a lower binding energy component due to $Cu^+$ formation after Au deposition over a $CuMnO_x$ sample. The simultaneous increase in the Mn/Cu surface atomic ratio was explained by the authors with preferential deposition of Au atoms on $Cu^{2+}$ sites [23].

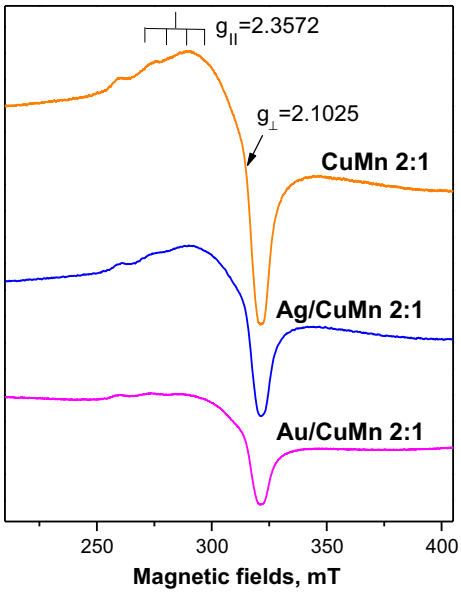


**Fig. 8** EPR spectra of the studied samples

The EPR spectra of all studied samples collected at RT are shown in Fig. 8. EPR spectroscopy was employed to obtain additional information on the nature of the active phase species. The spectrum of the Cu–Mn 2:1 catalyst displays an axial symmetry with four splitting features in the parallel region. Such hyperfine structure resulted from the coupling of the resonant spin with the magnetic moment of the copper nucleus with I = 3/2. The calculated g and A parameters were $g_{II} = 2.3572$, $g_{\perp} = 2.1025$, $A_{II} = 14mT$, $A_{\perp}$ was not resolved. This signal was assigned to isolated $Cu^{2+}$ ions in octahedral coordination with tetragonal distortion [43]. The appearance of this kind of hyperfine interaction may be related to a high dispersion of the corresponding paramagnetic ions [44]. The hyperfine splitting in perpendicular region is not resolved, probably because of antiferromagnetic dipolar interactions of paramagnetic $Cu^{2+}$ ions in small oxides clusters. The dipolar interactions between neighboring $Cu^{2+}$ ions cause the broadening of the individual EPR lines and therefore they cannot be observed. The analysis showed that copper (II) is present as a mixture of isolated $Cu^{2+}$ ions and aggregates of $Cu^{2+}$ ions. The lack of EPR signal characteristic for Mn species revealed that most likely they exist as $Mn^{4+}$. The shape of the EPR spectra was the same after deposition of Au and Ag on the surface, but the intensity of the EPR signal decreased and this effect was stronger in the spectrum of Au/Cu–Mn 2:1. The decreased intensity of the

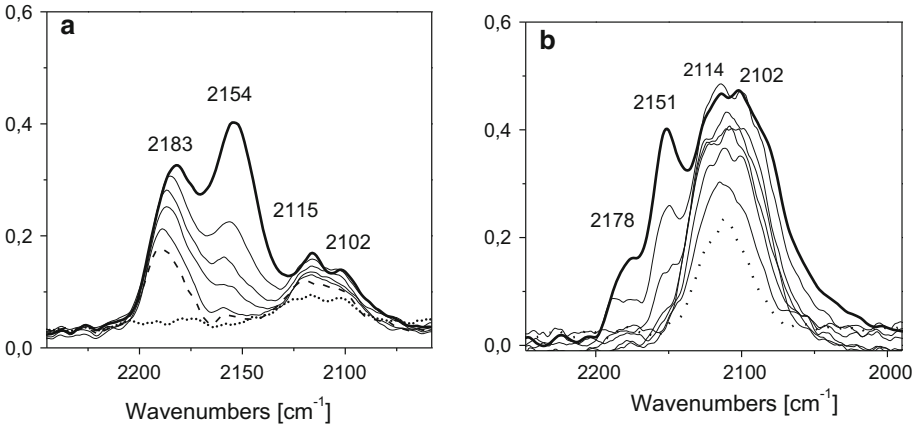


**Fig. 9** FTIR spectra of CO adsorbed on the alumina supported Cu–Mn 2:1 sample after an oxidative (section **a**) or reductive (section **b**) pretreatment: Section **a** *bold line* −4.5 mbar CO at −180 °C; *fine lines*—under outgassing at −180 °C; *dashed line*—after 20 min under outgassing at the same temperature and *dotted line*—under outgassing at increasing temperature; Section **b** *bold line* −6.9 mbar CO at −180 °C; *fine lines*—under outgassing at increasing temperature and *dotted line* under outgassing at RT

$Cu^{2+}$ signal is usually attributed to formation of EPR silent $Cu^{+}$ sites.

In order to study the state of surface species in real reaction conditions, FTIR spectra were collected after admission of CO at about −180 °C over alumina supported Cu–Mn 2:1 after an oxidative or reductive pretreatment (bold lines in Fig. 9, sections a and b, respectively). Different adsorption sites with different relative abundance are exposed depending on the thermal treatment atmosphere. CO adsorption on the oxidized Cu–Mn 2:1 sample revealed bands at 2183, 2154, 2115 and 2102 $cm^{-1}$. The band at 2183 $cm^{-1}$ is quite intense and gradually decreases in intensity, being reversible to the outgassing, whereas it is no more observed when the sample is submitted to a reductive treatment. This band can be assigned to CO adsorbed on $Mn^{3+}$ sites [45]. The band at 2154 $cm^{-1}$ is easily depleted upon outgassing at low temperature and it could be assigned to CO adsorbed in interaction with OH groups by hydrogen bond. However, a contribution to this absorption by $Cu^{2+}$ carbonyls cannot be excluded, being these species also usually poorly stable towards CO pressure reduction.

At lower frequency, the components at 2115 and 2102 $cm^{-1}$ can be assigned to CO on $Cu^{+}$ and $Cu^{0}$ species, respectively. Particularly, this kind of metallic copper sites is produced as a result of the fast reduction of highly dispersed Cu(II) sites by interaction with the CO probe admission, as evidenced by the simultaneous formation of a band at 2342 $cm^{-1}$ due to adsorbed $CO_2$ even at −180 °C (this band is not shown). These components become very intense when the sample is submitted to a reductive thermal treatment, indicating that a lot of copper species are at the surface and confirming the presence of $Cu^{2+}$ species on the oxidized sample (section b). The intense absorption is due to CO adsorbed on $Cu^{0}$ sites of small three dimensional copper particles [46], being the residual band observed after outgassing at r.t. due to $Cu^{+}$ carbonyls [47, 48]. A weak band at 2178 $cm^{-1}$, reasonably due to CO on $Mn^{2+}$ sites [45] produced by reduction of $Mn^{3+}$, together with a quite intense peak at 2151 $cm^{-1}$ and a broad and intense absorption with maxima at 2114 and 2102 $cm^{-1}$ already discussed, are produced when the Cu–Mn 2:1 sample is reduced in hydrogen. The peak at 2151 $cm^{-1}$ is again easily depleted under outgassing already at low temperature and it can be assigned to CO in interaction with OH groups, partially formed during the reduction in $H_2$.

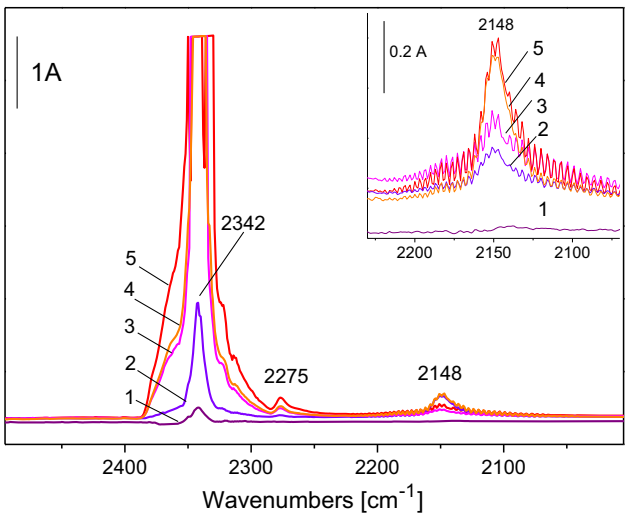


**Fig. 10** FTIR spectra collected upon admission of different amounts of CO at −180 °C over Au/Cu–Mn 2:1 after an oxidative pretreatment: *1*—with 4.4 mbar CO after 10 min, $P_{cell}$ = 40 mbar; *2*—with 50 mbar CO immediately, $P_{cell}$ = 55 mbar; *3*—with 50 mbar CO after 10 min, $P_{cell}$ = 88 mbar; *4*—with 100 mbar CO, immediately; *5*—with 100 mbar CO, after 10 min. *Inset* Zoom on the carbonylic region

To further investigate the state of surface species in real reaction conditions FTIR spectra were collected after admission of CO at –180 °C on Au/Cu–Mn 2:1 after an oxidative pretreatment (Fig. 10). However, upon inlet of CO the pressure continuously increased, together with formation of large amount $CO_2$ (bands out of scale). Therefore, it was proposed that $CO_2$ is both adsorbed as well as in the gas phase. More detailed inspection of the carbonylic region (see inset) revealed that small amounts of CO probe are adsorbed and quickly consumed to produce $CO_2$. It should be noted that the same experiment performed with alumina supported Cu–Mn 2:1 put in evidence different Cu and Mn sites (Fig. 9, section a). The presence of gold strongly affects the nature of the exposed sites and their adsorption capability, due to the extremely enhanced reactivity towards CO oxidation. Very high CO oxidation activity of Au/Cu–Mn sample could be related to the presence of adsorbed oxygen (possibly on the highly dispersed Au particles with size around 1 nm, observed by HRTEM) and to the very good redox properties of the mixed Cu–Mn oxide support. These results are consistent with the finding by Sandoval et al. about the role of the activation procedure on the CO oxidation activity of Au–$Cu/TiO_2$ catalysts [49]. The authors have shown that the activation in air at 300 °C produced more active catalysts than the activation under hydrogen at the same temperature. By using DRIFTS they have found that after treatment in air gold was present in metallic form, copper as an oxide, while bimetallic particles were produced after reduction. The FTIR experiments of adsorbed CO in the present study confirm the availability of metallic gold and CuO particles on the oxidized sample, however bimetallic particles were not found.

The spectra collected upon CO inlet at −180 °C over the Au/Cu–Mn 2:1 catalyst upon reduction treatment clearly explained the lower reactivity of the sample. Indeed, different bands in the carbonylic region were distinguished after CO admission (Fig. 11, fine line). In particular, a band at 2112 $cm^{-1}$ could be assigned to CO adsorbed on $Cu^0$ sites, due to its decreased intensity after outgassing (bold line) as well as to its almost total depletion upon $O_2$ inlet and outgassing, as shown in the following Fig. 12. The further inlet of $O_2$ produced $CO_2$ and the band at 2113 $cm^{-1}$ was consumed under outgassing (Fig. 12). The residual band (dashed dotted line) was resistant to the outgassing at RT and it can be due to $Cu^+$ species, because of the higher resistance of Cu(I) carbonyls in comparison with Cu(0) carbonyls [45]. Moreover, an isosbestic point was observed by increasing the temperature under outgassing (fine lines), most probably due to the presence of gold carbonyls. These results are in good agreement with XPS and EPR data for the availability of highly dispersed gold particles and $Cu^{2+}$ sites with high reactivity. These copper sites are able to undergo very fast reduction after interaction with CO.

The analysis of the redox properties of the catalysts can contribute to a better interpretation of the catalytic results. The $H_2$-TPR profiles of the samples are shown in Fig. 13. For comparison, those of CuO and MnOx both supported on alumina are also presented. According to the literature data, the reduction of bulk CuO proceeds in a single step process with peak maximum about 300 °C. In the present study, the reduction profile of supported single copper oxide is complex with two components ($T_{max}$ at 197 and 248 °C). According to the literature, these two peaks should be related to the reduction of $Cu^{2+} \rightarrow Cu^+$ and

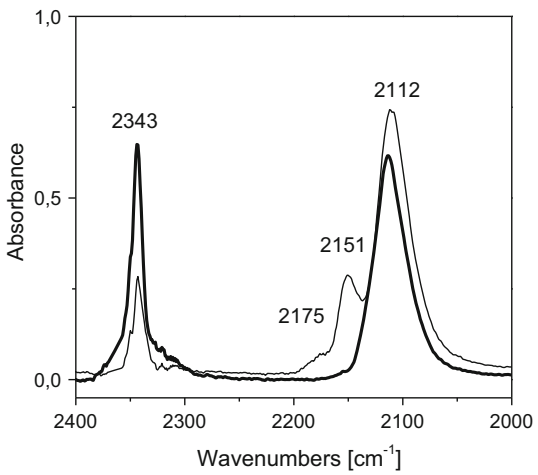


**Fig. 11** FTIR spectra collected upon admission of 4.5 mbar CO at −180 °C over reduced Au/Cu–Mn 2:1 (*fine line*) and after outgassing (*bold line*)

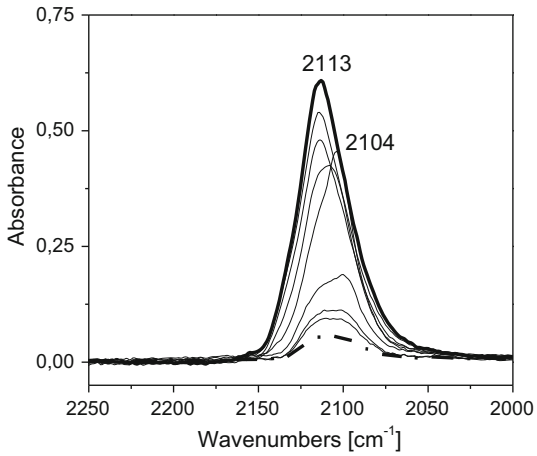


**Fig. 12** FTIR spectra collected upon admission of 50 mbar $O_2$ at −180 °C over Au/Cu–Mn 2:1 after outgassing (*bold line*) and under outgassing at increasing temperature (*fine lines*) up to RT (*bold dashed dotted line*)

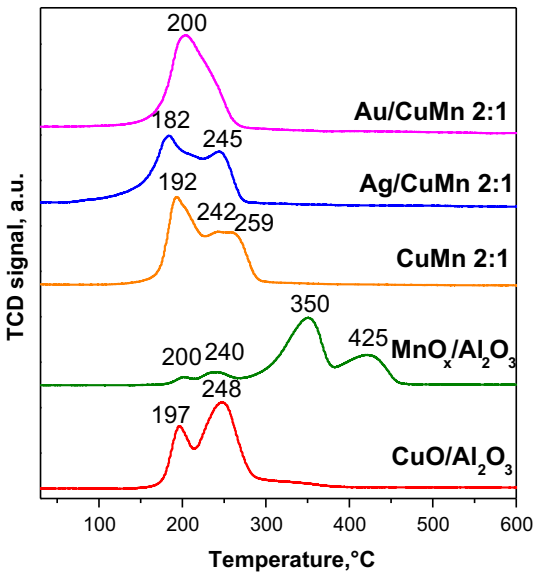


**Fig. 13** Temperature programmed reduction profiles of the samples

$Cu^{+} \rightarrow Cu^{0}$ [50]. Here, such an interpretation seems less likely since both components have quite different intensity. Some authors explained the complex profile with the existence of two reducible CuO species: the low-temperature part is attributed to finely dispersed CuO particles, the high-temperature part is due to large particles of bulk CuO [51]. The downshift of $T_{max}$ in comparison with the temperature reported for bulk CuO indicated that the preparation procedure applied in this study facilitates the formation of CuO particles with improved reducibility. The reduction of pure $Mn_2O_3$ proceeds also in step-wise route and is generally ascribed to the following reduction steps: $MnO_2 \rightarrow Mn_2O_3 \rightarrow Mn_3O_4 \rightarrow MnO$ [20]. The profile of the supported Cu–Mn 2:1 sample displays features similar to the profile of $CuO/Al_2O_3$, as for the complex shape and the position of the two components. However, the more intense peak in the low-temperature part of the profile related to the mixed oxide sample may be assigned to the reduction of highly dispersed CuO particles. The second complex and broad component centered at 242 and 259 °C was related to the reduction of the big CuO particles and of the Cu–Mn spinel phase. This assignment is consistent with the interpretation of the EPR data for the existence of two types of $Cu^{2+}$ sites, due to the presence of isolated Cu(II) ions and aggregates of CuO. On the other hand, by XPS was confirmed the presence of $Mn^{4+}$ and these ions are reduced at temperature lower than that of $Mn^{3+}$ [20]. The deposition of Au altered the complex shape of the peak and improved the reducibility of the mixed oxides. Indeed, the addition of Au boosted the reduction of the spinel phase, that is completed at a lower temperature if compared to the bare Cu/Mn 2:1 sample. The enhanced reduction of the spinel phase after doping with Au could be explained by the occurrence of hydrogen activation on nanosized gold particles and subsequent spillover of atomic hydrogen onto the support [52]. In addition, a FTIR study on gold-based catalysts showed that the dissociation of hydrogen could occur at room temperature on gold sites and these hydrogen atoms could reduce the surface sites [53]. The ease of reducibility of the spinel phase in the presence of Au could be interpreted in terms of improved oxygen mobility with the consequent formation of oxygen vacancies, and correlates with the best CO oxidation activity of this catalyst. In contrast to the highly favorable role of Au, the addition of Ag caused only slight effect on the reduction behavior.

The discussion on structure–reactivity relationship of alumina supported Cu–Mn mixed oxides with Cu/Mn molar ratio 2:1 after addition of Au or Ag showed that the deposition of highly dispersed gold particles led to a considerable enhancement of the CO and methanol oxidation activity, while doping with Ag caused negligible effect. The superior performance of Au/Cu–Mn sample might be explained with cooperative effects in adsorption and activation of oxygen and CO or VOC molecules. According to some experimental and theoretical works, the adsorption and activation of oxygen play an important role in CO oxidation. The ability of Au to adsorb CO on corner, edge, borderline or cluster sites in gold nanostructured catalysts is strongly dependent on the type of support [54]. In this sense, the Cu–Mn oxide support with good redox properties contributed for oxygen activation and the combination with gold nanoparticles resulted in a remarkable improvement of the catalytic behavior. The reason for significant differences in CO oxidation activity of gold- and silver-promoted samples might be explained by the worse oxidizing capabilities of silver compared to gold. In comparative study of IB metals (Au, Ag and Cu) supported on $TiO_2$, the very low activity of $Ag/TiO_2$ in the water–gas shift reaction was related to the incapability of silver in the CO chemisorption and activation [55]. The same findings were reported by Scirè et al. after investigation of PROX reaction over IB metal/$CeO_2$ catalysts. In this case Au and Cu catalysts demonstrated high CO conversions ($Au/CeO_2$ at low temperatures, $Cu/CeO_2$ at higher temperatures), whereas $Ag/CeO_2$ catalysts attained very low CO conversion in a whole temperature range [56]. The study of catalytic combustion of methanol over IB metal/$CeO_2$ catalysts demonstrated the following activity order: $Au/CeO_2 \geq Ag/CeO_2 > Cu/CeO_2 \gg CeO_2$ [56]. The authors have found the same order analyzing the promotional role of IB metal on the reducibility of ceria lattice oxygen species. Following the general opinion that VOC deep oxidation over metal catalysts supported on reducible oxides occurs through a Mars–van Krevelen mechanism, the main role for enhancement of the reducibility was attributed to the ability of the IB metal to weaken the Ce–O

bond located nearby the active metal atoms. The TPR measurements in the present work demonstrated the beneficial role of Au to enhance reduction of the Cu–Mn mixed oxides, while the addition of Ag has only a slight effect on the reducibility. The differences in the reduction behavior also contribute for different catalytic performance of Au- and Ag-based samples.

## 4 Conclusions

The promotional effect of Au or Ag addition to alumina supported Cu–Mn mixed oxide with molar ratio 2:1 on the structural, electronic, reductive and catalytic properties for the oxidation of CO, methanol and dimethylether was investigated. The analysis of the structural characteristics and of the catalytic performance showed that the deposition of highly dispersed gold particles led to a considerable enhancement of CO and methanol oxidation activity, while doping with Ag caused insignificant effect. The effect of Au could be related to the appearance of new active sites, able to interact with CO, as well as to the improvement of the redox properties of the Cu–Mn spinel, that influences the mobility of lattice oxygen. The catalytic tests related to the simultaneous oxidation of CO, $CH_3OH$ and DME put in evidence the promising behavior of the Au-promoted catalyst. The combination of the favorable features of Cu–Mn mixed oxides with those of gold nanoparticles represents an advantageous approach for developing new catalytic formulations with high effectiveness for the elimination of different type pollutants in waste gases. The use of a high surface area support is beneficial for the stabilization of gold particles in a highly dispersed state. Additionally, the composition of this catalytic system which is mostly composed of alumina (80 %) is advantageous in practical applications because of its economic viability.

**Acknowledgments** The authors affiliated at Institute of Catalysis and Agricultural University gratefully acknowledge financial support by the Bulgarian Science Fund (Project DFNI T 02/4). T.T., A.M.V. and P.P. are thankful to COST Action CM1104.

## References

1. Huang H, Xu Y, Feng Q, Leung DYC (2015) Catal Sci Techn 5:2649–2669 **(references therein)**
2. Carabineiro SAC, Chen X, Martynyuk O, Bogdanchikova N, Avalos-Borja M, Pestryakov A, Tavares PB, Órfão JJM, Pereira MFR, Figueiredo JL (2015) Catal Today 244:103–114
3. Liotta LF (2010) Appl Catal B 100:403–412
4. Barakat T, Rooke JC, Genty E, Cousin R, Siffert S, Su BL (2013) Energy Envirn Sci 6:71–391
5. Avgouropoulos G, Tabakova T (2013) Environmental catalysis over gold-based materials. RSC catalysis series No 13, RSC Publishing, Thomas Graham House, Cambridge
6. Scirè S, Liotta LF (2012) Appl Catal B 125:222–246
7. Stoyanova M, Petrov D, Dimitrov D, Ivanov K, Christoskova S (2014) J Int Sci Publ Ecol Saf 8:479–486
8. Delimaris D, Ioannides T (2008) Appl Catal B 84:303–312
9. Liotta LF, Wu HJ, Pantaleo G, Venezia AM (2013) Catal Sci Technol 3:3085–3102
10. Tsoncheva T, Issa G, Blasco T, Dimitrov M, Popova M, Hernández S, Kovacheva D, Atanasova G, López Nieto JM (2013) Appl Catal A 453:1–12
11. Aguilera DA, Perez A, Molina R, Moreno S (2011) Appl Catal B 104:144–150
12. Hutchings GJ, Mirzaei AA, Joyner RW, Siddiqui MRH, Taylor SH (1996) Catal Lett 42:21–24
13. Hutchings GJ, Mirzaei AA, Joyner RW, Siddiqui MRH, Taylor SH (1998) Appl Catal A 166:143–152
14. Krämer M, Schmidt T, Stöwe K, Maier WF (2006) Appl Catal A 302:257–263
15. Cai L, Hu Z, Branton P, Li W (2014) Ch J Catal 35:159–167
16. Clarke TJ, Davies TE, Kondrat SA, Taylor SH (2015) Appl Catal B 165:222–231
17. Larsson PO, Andersson A (2000) Appl Catal B 24:175–192
18. Behar S, Gonzalez Ph, Agulhon P, Quignard F, Swierczynski D (2012) Catal Today 189:35–41
19. Li X, Wang L, Xia Q, Liu Z, Li Z (2011) Catal Commun 14:15–19
20. Morales MR, Barbero BP, Cadús LE (2006) Appl Catal B 67:229–236
21. Morales MR, Barbero BP, Cadús LE (2008) Fuel 87:1177–1186
22. Solsona B, Hutchings GJ, Garcia T, Taylor SH (2004) New J Chem 28:708
23. Cole KJ, Carley AF, Crudace MJ, Clarke M, Taylor SH, Hutchings GJ (2010) Catal Lett 138:143–147
24. Solsona B, Garcia T, Agouram S, Hutchings GJ, Taylor SH (2011) Appl Catal B 101:388–396
25. Lamb AB, Bray WC, Fraser CW (1920) J Ind Chem Eng 12:213
26. Ivanov K, Kolentsova E, Dimitrov D (2015) Int J Chem Nucl Mater Metallurg Eng 9:548–557
27. Grisel RJH, Kooyman PJ, Nieuwenhuys BE (2000) J Catal 191:430–437
28. Ivanova S, Petit C, Pitchon V (2006) Catal Today 113:182–186
29. Ousmane M, Liotta LF, Di Carlo G, Pantaleo G, Venezia AM, Deganello G, Retailleau L, Boreave A, Giroir-Fendler A (2011) Appl Catal B 101:629–637
30. Ivanov K, Dimitrov D, Boyanov B (2009) Chem Eng J 154:189–195
31. Ivanov K, Kolentsova E, Dimitrov D, Avdeev G, Tabakova T (2015) WASET. Int J Chem Molec Nucl Mater Metallurg Eng 9:669–674
32. Wei P, Bieringer M, Cranswick LMD, Petric A (2010) J Mater Sci 45:1056–1064
33. Kondrat SA, Davies TE, Zu Z, Boldrin P, Bartley JK, Carley AF, Taylor SH, Rosseinsky MJ, Hutchings GJ (2011) J Catal 281:279–289
34. Papavasiliou J, Avgouropoulos G, Ioannides T (2007) J Catal 251:7
35. Biesinger MC, Payne BP, Grosvenor AP, Lau LWM, Gerson AR, Smart RSC (2011) Appl Surf Sci 257:2717–2730
36. Longo A, Liotta LF, Di Carlo G, Giannici F, Venezia AM, Martorana A (2010) Chem Mater 22:3952–3960
37. Tabakova T, Dimitrov D, Manzoli M, Vindigni F, Petrova P, Ilieva L, Zanella R, Ivanov K (2013) Catal Commun 35:51–58
38. Casaletto MP, Longo A, Martorana A, Prestianni A, Venezia AM (2006) Surf Interface Anal 38:215–218
39. Fierro-Gonzalez JC, Guzman J, Gates BC (2007) Top Catal 44:103–114
40. Minico S, Scire S, Crisafulli C, Galvagno S (2001) Appl Catal B 34:277–285

41. Nikolaev SA, Golubina EV, Krotova IN, Shilina MI, Chistyakov AV, Kriventsov VV (2015) Appl Catal B 168:303–312
42. Duh FC, Lee DS, Chen YW (2013) Mod Res Catal 2:1–8
43. Ratnasamy P, Srinivas D, Satyanarayana CVV, Manikandan P, Kumaran RSS, Sachin M, Shetti VN (2004) J Catal 221:455–465
44. Ramaswamy V, Bhagwat M, Srinivas D, Ramaswamy AV (2004) Catal Today 97:63–70
45. Hadjiivanov KI, Vayssilov GN (2002) Adv Catal 47:307–511
46. Boccuzzi F, Ghiotti G, Chiorino A (1985) Surf Sci 156:933–942
47. Manzoli M, Di Monte R, Boccuzzi F, Coluccia S, Kašpar J (2005) Appl Catal B 61:192–205
48. Colonna F, Marquez F, Rochester CH, Anderson JA (2000) PCCP 2:5320–5327
49. Sandoval A, Louis C, Zanella R (2013) Appl Catal B 140:363–377
50. Cao H, Li X, Chen Y, Gong M, Wang J (2012) Rare Earths 30:871–877
51. Kundakovic L, Flytzani-Stephanopoulos M (1998) Appl Catal A 171:13–29
52. Manzoli M, Chiorino A, Vindigni F, Boccuzzi F (2012) Catal Today 181:62–67
53. Boccuzzi F, Chiorino A, Manzoli M, Andreeva D, Tabakova T (1999) J Catal 188:176–185
54. Vindigni F, Manzoli M, Chiorino A, Boccuzzi F (2009) Gold Bull 42:106–112
55. Boccuzzi F, Chiorino A, Manzoli M, Andreeva D, Tabakova T, Ilieva L, Idakiev V (2002) Catal Today 75:169–175
56. Scire S, Riccobene PM, Crisafulli C (2010) Appl Catal B 101:109–117